

## Controlling the Vaterite $\text{CaCO}_3$ Crystal Pores. Design of Tailor-Made Polymer Based Microcapsules by Hard Templating

Natalia Feoktistova,<sup>†,‡</sup> Juergen Rose,<sup>§</sup> Vladimir Z. Prokopović,<sup>†</sup> Anna S. Vikulina,<sup>†,||</sup> Andre Skirtach,<sup>⊥</sup> and Dmitry Volodkin<sup>\*,†,‡,||</sup>

<sup>†</sup>Branch Bioanalytics and Bioprocesses (Fraunhofer IZI-BB), Fraunhofer Institute for Cell Therapy and Immunology, Am Muehlenberg 13, 14476 Potsdam-Golm, Germany

<sup>‡</sup>Department of Chemistry, Lomonosov Moscow State University, Leninskiye gory 1-3, 119991 Moscow, Russia

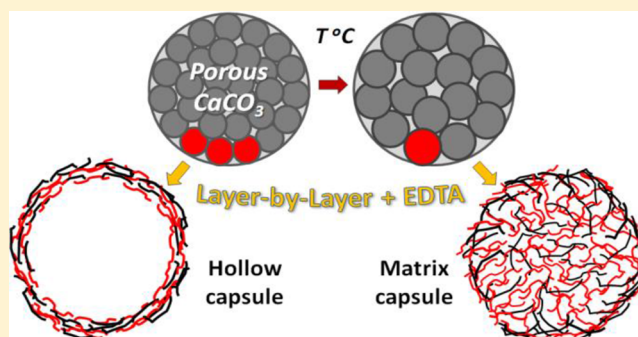
<sup>§</sup>Institute for Biochemistry and Biology, University of Potsdam, Karl-Liebknecht-Str. 24-25, 14476 Potsdam-Golm, Germany

<sup>||</sup>School of Science and Technology, Nottingham Trent University, Clifton Lane, Nottingham NG11 8NS, United Kingdom

<sup>⊥</sup>Department of Molecular Biotechnology & NB-Photonics, University of Ghent, Coupure Links 653, 9000 Gent, Belgium

### Supporting Information

**ABSTRACT:** The spherical vaterite  $\text{CaCO}_3$  microcrystals are nowadays widely used as sacrificial templates for fabrication of various microcarriers made of biopolymers (e.g., proteins, nucleic acids, enzymes) due to porous structure and mild template elimination conditions. Here, we demonstrated for the first time that polymer microcarriers with tuned internal nanoarchitecture can be designed by employing the  $\text{CaCO}_3$  crystals of controlled porosity. The layer-by-layer deposition has been utilized to assemble shell-like (hollow) and matrix-like (filled) polymer capsules due to restricted and free polymer diffusion through the crystal pores, respectively. The crystal pore size in the range of few tens of nanometers can be adjusted without any additives by variation of the crystal preparation temperature in the range 7–45 °C. The temperature-mediated growth mechanism is explained by the Ostwald ripening of nanocrystallites forming the crystal secondary structure. Various techniques including SEM, AFM, CLSM, Raman microscopy, nitrogen adsorption–desorption, and XRD have been employed for crystal and microcapsule analysis. A three-dimensional model is introduced to describe the crystal internal structure and predict the pore cutoff and available surface for the pore diffusing molecules. Inherent biocompatibility of  $\text{CaCO}_3$  and a possibility to scale the porosity in the size range of typical biomacromolecules make the  $\text{CaCO}_3$  crystals extremely attractive tools for template assisted designing tailor-made biopolymer-based architectures in 2D to 3D targeted at drug delivery and other bioapplications.



## INTRODUCTION

A variety of different strategies have been exploited to assemble organic, inorganic, and hybrid materials with well-defined architectures by utilizing molecular self-organization into superstructures.<sup>1–3</sup> Hard templating<sup>1,2,4–6</sup> method is one of the main approaches to assemble such structures, and it is based on infiltration of a decomposable template with material of interest followed by template removal resulting in the formation of an inverse replica of the template. What makes this technique particularly versatile is the fact that material parameters of the formed structures can be tuned by the properties of the decomposable templates, namely, by shape, size, and internal structure.

In the past decade, the hard templating approach based on decomposable, porous  $\text{CaCO}_3$  crystals<sup>7</sup> has been extensively used for fabrication of microcarriers (beads and capsules) containing various bioactive compounds.<sup>8–12</sup> Nowadays this type of porous inorganic crystal (the vaterite form of  $\text{CaCO}_3$ ) is

one of the most popular approaches for encapsulation of bioactive molecules due to mild decomposition conditions (pH below neutral or EDTA) and large internal surface. Alternative sacrificial particles such as colloids made of melamine formaldehyde,<sup>13,14</sup> silica,<sup>15–17</sup> polystyrene, and polylactic acids<sup>18</sup> are not well suited for bioapplications because of harsh conditions needed to eliminate these particles: low pH (below 1), HF, organic solvents, and HClO, respectively. On the other hand, an incomplete template elimination may limit the use of the decomposable organic cores.<sup>13,14</sup> In addition to mild dissolution conditions, another notable advantage of the  $\text{CaCO}_3$  crystals is a relatively easy production in the lab from inexpensive and widely accessible salt precursors,  $\text{CaCl}_2$  and  $\text{Na}_2\text{CO}_3$ . Additionally, rather low polydispersity, control over

Received: February 24, 2016

Revised: April 6, 2016

Published: April 6, 2016

crystal size (in the micrometer and submicrometer range<sup>19,20</sup>), and crystal shape<sup>21</sup> make such crystals an attractive candidate for a variety of applications.

Encapsulation of various biomolecules including small drugs and large biomacromolecules by CaCO<sub>3</sub> templating is a simple two-step process.<sup>8</sup> First, the biomolecules are immobilized in the pores of the CaCO<sub>3</sub> crystals, accomplished by physical adsorption,<sup>19,22–24</sup> chemical cross-linking,<sup>25–27</sup> coprecipitation,<sup>28–32</sup> and trapping by coating with polyelectrolyte multilayers.<sup>24,31,33–35</sup> The second step includes subsequent crystal dissolution (pH below neutral or EDTA) resulting in the formation of the microparticles with encapsulated biomolecules. A crucial step in the encapsulation is immobilization of molecules, because that determines the loading efficiency. The distribution of the immobilized molecules defines the structure of the formed microcarrier (true capsule, matrix-type capsule, compact or porous bead) as well as the amount of loaded biomolecules.<sup>5</sup> Evidently this distribution depends on molecular transport into the crystal pores. Despite of its role in biomolecule encapsulation by templating on CaCO<sub>3</sub> crystals, to the best of our knowledge, no control over the pore size of the pure CaCO<sub>3</sub> crystals has been shown.

Such environmental conditions as pH, ionic strength, and additives, including organic and inorganic substrates, are known to significantly affect the crystallization process of CaCO<sub>3</sub> crystals.<sup>36–45</sup> It is known from literature that temperature variation during CaCO<sub>3</sub> crystallization has a strong effect leading to crystallization of a certain polymorphous form.<sup>46,47</sup> However, no influence of the ambient temperature on the porosity of vaterite polymorphs has been reported. In this work we demonstrate that the porosity of the CaCO<sub>3</sub> crystals can be adjusted without any additives by means of temperature variation during the crystal growth. We explain this effect by the temperature mediated spherulitic growth mechanism<sup>48</sup> of the vaterite CaCO<sub>3</sub> crystals. To demonstrate the formation of polymeric microcapsules templated on CaCO<sub>3</sub> crystals of varied porosity we have assembled shell-like and matrix-like LbL microcapsules. The structures of CaCO<sub>3</sub> crystals and the assembled capsules have been analyzed by scanning electron microscopy (SEM), confocal laser scanning microscopy (CLSM), and nitrogen adsorption–desorption by Brunauer–Emmett–Teller method (BET).

## EXPERIMENTAL SECTION

**Materials.** Calcium chloride dihydrate (CaCl<sub>2</sub>·2H<sub>2</sub>O), sodium carbonate anhydrous (Na<sub>2</sub>CO<sub>3</sub>), dextran labeled with fluorescein isothiocyanate (dextran-FITC) of 10 and 70 kDa, fluorescein isothiocyanate (FITC, Sigma-Aldrich, Germany), and poly(sodium 4-styrenesulfonate) (PSS) and poly(allylamine hydrochlorid) (PAH) (both 70 kDa) were purchased from Sigma-Aldrich (Germany). PAH-FITC has been labeled with FITC at a molar ratio of 1:100 (FITC to PAH polymer units) in 0.1 M carbonate buffer, pH 9.0 (room temperature, incubation time 2 h) followed by dialysis in water. The water used in all experiments was prepared via a Millipore Milli-Q purification system and had a resistivity higher than 18.2 MΩ cm.

**CaCO<sub>3</sub> Crystal Preparation.** CaCO<sub>3</sub> crystals were synthesized according to the protocol described in refs 7 and 19 with some changes in the protocol. Briefly, 3 mL of 1 M Na<sub>2</sub>CO<sub>3</sub> were rapidly added to 12 mL of 0.2 M CaCl<sub>2</sub> solution. The mixture was intensively agitated on a magnetic stirrer (160 rpm) during 30 s. The preparation temperature was set 7.5, 22, and 45 °C. Particle growth time has been 60, 80, and 30 min for 7.5, 22, and 45 °C, respectively. The amorphous precipitate formed upon the mixing has been further transformed into crystals. The grown crystals were rinsed thoroughly three times with

water. The supernatant was removed by decantation; the crystals were dried at 90 °C overnight and stored at room temperature.

**Fabrication of Multilayer Microcapsules.** First the CaCO<sub>3</sub> crystals have been coated by PSS and PAH using layer-by-layer approach. Then 10 mg of CaCO<sub>3</sub> crystals was suspended in 1 mL of either PAH or PSS solutions (0.5 mg/mL) followed by 10 min incubation under agitation. Afterward the suspension was centrifuged (1 min, 2000 g) and supernatant was removed. For the next washing step, the sediment was redispersed in 1 mL of water on vortex, centrifuged (1 min, 2000g), and redispersed again in 1 mL of water. The washing step has been repeated three times. Further deposition of the next polymer (PSS) has been performed similarly to that of PAH. Washing steps in between polymer deposition were always done. Finally 12 polymer deposition steps resulted in the structure (PAH/PSS)<sub>6</sub>.

**Confocal Laser Scanning Microscopy (CLSM).** CLSM images were obtained on Zeiss LSM 510 Meta (Zeiss, Germany) instrument. It was used to image retinal whole mounts and sections with 40× (Plan-Neofluar, NA 1.3, Zeiss, Germany) or 63× (Plan-Apochromat, NA 1.4, Zeiss, Germany) oil-immersion objectives. Standard filter settings for excitation and emission of FITC were used for a laser source of 488 and for transmission 633 nm. Images were processed in Image Pro (Adobe Systems Inc.) to enhance brightness and color. For crystal permeability study, 0.5 mL (0.1 mg/mL) of dextran-FITC solution was added to 1 mg of crystals followed by fluorescence analysis after 15, 30, and 60 min.

**Scanning Electron Microscopy (SEM).** For SEM analysis, samples have been prepared by applying a drop of the crystal suspension in water to a glass slide followed by drying 1 h at 90 °C. The samples were sputtered with gold and the measurements were conducted using a Gemini Leo 1550VP (Zeiss, Germany) instrument at operation voltage of 3 keV. Morphology of the crystal surface has been analyzed by taking gray scale profiles from SEM images using a program Image Pro. To get an average value between minimums in the obtained profiles, 34, 30, and 34 peaks have been analyzed for the crystals prepared at 7.5, 22, and 45 °C, respectively.

**Raman Microscopy.** For taking Raman spectra of the prepared CaCO<sub>3</sub> crystals, a Raman microscope (CRM200, WITec, Ulm, Germany) equipped with a piezo-scanner (P-500, Physik Insrtumente, Karlsruhe, Germany) and diode-pumped 785 nm NIR laser excitation (Toptica Photonics AG, Graefelfing, Germany) has been used. The laser beam was focused through a 100× (NA 0.95, Olympus) objective. The spectra were acquired with a thermoelectrically cooled CCD detector (DU401ABV, Andor, U.K.) behind a grating (300 g mm<sup>-1</sup>) spectrograph (Action, Princeton Instruments Inc., Trenton, NY) with a spectral resolution of 6 cm<sup>-1</sup>.

**Analysis of the Crystal Surface Area.** To measure surface area of the prepared crystal, N<sub>2</sub> adsorption–desorption analyses were performed using a QUADRASORB SI-MP (Quantachrome Instruments) instrument at 77.3 K. Prior to measurement, the samples were degassed (150 °C, 20 h). Brunauer–Emmett–Teller (BET) theory and the Barrer–Joyner–Halenda model were used for surface area and pore-size distribution analysis, respectively.

**X-ray Diffraction Analysis (XRD).** X-ray diffraction patterns were recorded using an X-ray powder diffractometer D8 ADVANCE (Bruker AXS, Germany). The XRD analysis were performed in symmetrical reflection mode with Cu Kα radiation (λ = 1.5418 Å) using Gobel Mirror bent gradient multilayer optics. The abundance of two polymorphs vaterite and calcite was calculated from the areas of the main diffraction peaks (Figure S4) of vaterite (at 27.0° 2θ) and calcite (at 29.4° 2θ), using Origin 8.1.

**Atomic Force Microscopy (AFM) Measurements.** AFM measurements were done on a “Nanowizard I” atomic force microscope (JPK Instruments AG, Berlin, Germany). Integral particles were firmly fixed to a glass slide with or without prior breaking of particles, depending on the requirements of the experiment. Particles of interest were identified using phase contrast optics (objective 20×, NA 0.45 A-Plan, Carl Zeiss AG, Germany) and imaged in air in tapping mode with OMCL-AC160BN-A2 cantilevers (Olympus, Japan). Data were evaluated with Gwyddion software.

## RESULTS AND DISCUSSION

**Synthesis of Mesoporous  $\text{CaCO}_3$  Crystals.** Recently control over  $\text{CaCO}_3$  crystal size (in the range 3–15  $\mu\text{m}$ )<sup>19</sup> has been demonstrated by variation of a number of the formed nuclei during the crystal growth at supersaturation conditions by mixing of  $\text{CaCl}_2$  and  $\text{Na}_2\text{CO}_3$ . This has been achieved by changing the stirring time and the stirring speed during salt mixing due to heterogeneous nucleation mechanism (nuclei are formed on the liquid–solid interface). However, the synthesis does not result in porosity change of the formed crystals. The prepared crystals are found to have mesoporous structure with the average pore size of about 25–30 nm.<sup>19</sup>

In order to investigate control over the porosity of the  $\text{CaCO}_3$  crystals some parameters can be readily tuned during the crystal growth. At the same time, we have excluded additives which are known to significantly affect the crystallization process.<sup>36–38</sup> Additive-free synthesis is preferred in order to avoid any additional and sometimes complicated steps of the additive removal. The temperature during the  $\text{CaCO}_3$  crystal preparation has been identified as one of the tuning parameters.

We have prepared  $\text{CaCO}_3$  crystals using a standard procedure<sup>7,19</sup> based on mixing of precursor salts ( $\text{Na}_2\text{CO}_3$  and  $\text{CaCl}_2$ ) at varied temperatures, e.g., 7.5, 22, and 45 °C. SEM images of the prepared crystals are presented in Figure 1A–C. The size of the crystals was found to be affected by the

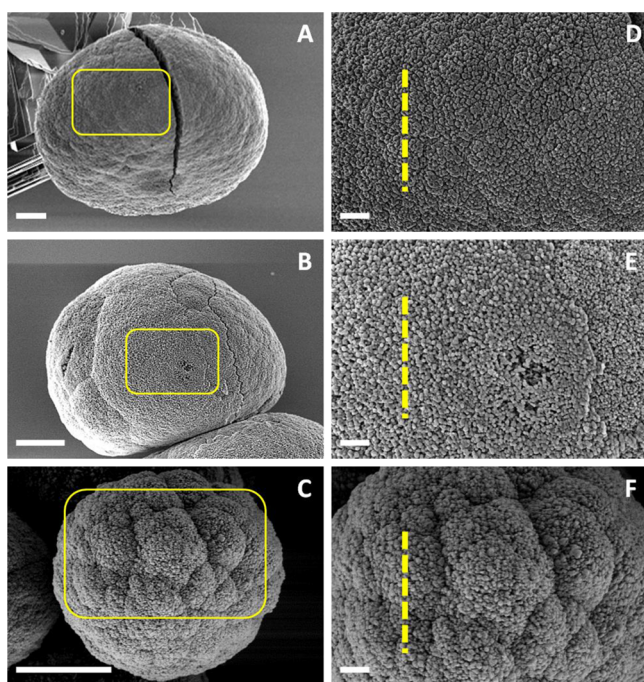


**Figure 1.** SEM images of  $\text{CaCO}_3$  crystals grown at 7.5 °C (A), 22 °C (B), and 45 °C (C). SEM images (D)–(F) represent the enlarged areas (depicted in yellow) of images (A)–(C), respectively. Scale bar for (A)–(C) is 5  $\mu\text{m}$ , and that for (D)–(F) is 1  $\mu\text{m}$ .

preparation temperature. The diameters of the crystals grown at 7.5, 22, and 45 °C are in the range of 30–50, 15–30, and 9–13  $\mu\text{m}$ , respectively (Figure S1). Most probably the observed decrease of the crystal size with increased ambient preparation temperature is related to a higher number of nuclei formed at higher temperature. Since the amount of ions for crystal growth is kept similar, a large number of the formed nuclei will reduce

the final size of the grown crystal. However, not all samples are monodispersed. In order to compare the crystal structure between each other, we have considered crystals of comparable sizes, e.g., in the range of 10–20  $\mu\text{m}$  (Figure 1A–C).

**Analysis of  $\text{CaCO}_3$  Crystal Structure.** To analyze the crystal structure, we have first focused on the crystal surface morphology. Primary vaterite crystals have a secondary structure and are thus called polycrystallites. They are composed of crystallites which have a size in the range of nanometers.<sup>48,49</sup> Detailed analysis of the surface of the crystals formed in this study has revealed that the nanocrystallites represent rather spherical particles aggregated to each other and forming a complex secondary structure (Figure 1). The size of the nanocrystallites on the crystal surface is increased for the crystals grown at higher temperature (Figure 1D–F). Figure 2A shows a gray scale profile taken from the SEM images of the crystal surfaces. It is obvious that the amplitude of the profiles and the distance between the peaks are proportional to dimensions of the nanocrystallites as typical features of the crystal surface. One can clearly conclude from the profiles

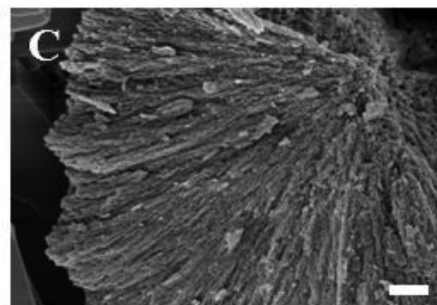
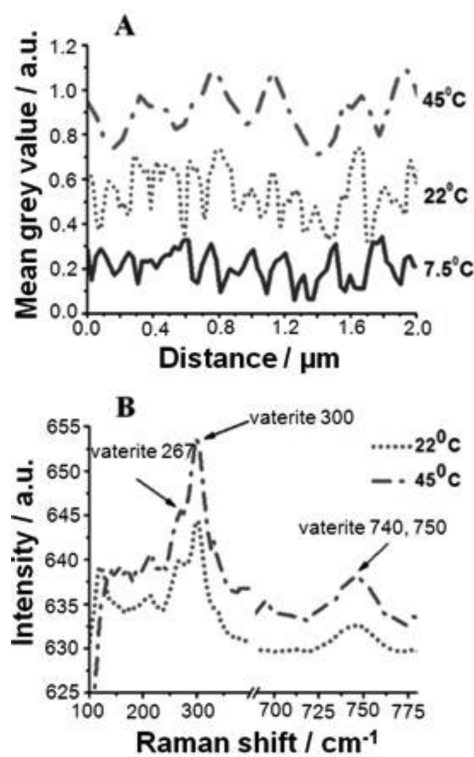


**Figure 2.** (A) Profiles of surfaces along yellow interrupted lines in Figure 1D–F. (B) Raman spectra of  $\text{CaCO}_3$  particles at different temperatures. (C) SEM image of broken particle. Scale bar for (C) is 1  $\mu\text{m}$ .

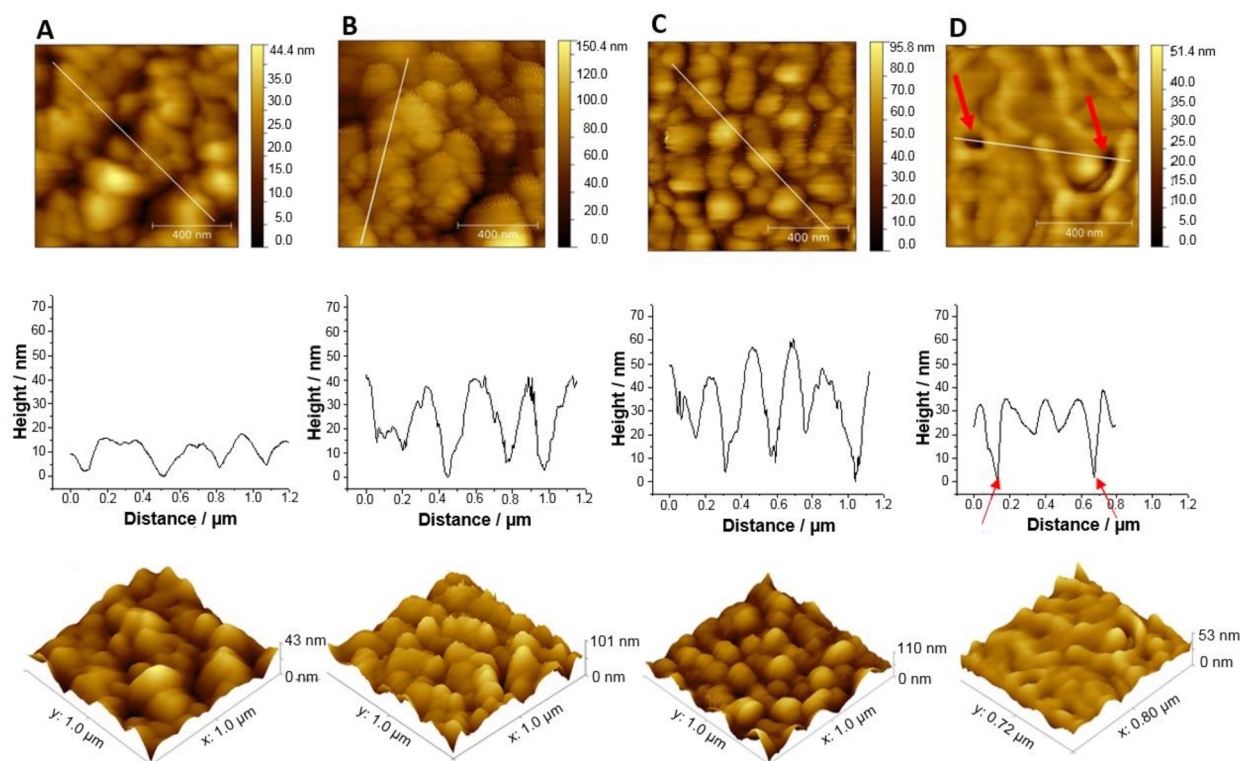


**Figure 3.** AFM images of the  $\text{CaCO}_3$  crystals. (A–C) Surface imaging of the crystals prepared at 7.5, 22, and 45 °C, respectively. (D) Image of the broken crystal prepared at 7.5 °C (internal surface analyzed). AFM images are supported by cross section profiles taken along the white lines shown in images (A)–(D) as well as three-directional profiles, both placed underneath images (A)–(D).

(Figure 2A) that within an increase of the preparation temperature the size of the nanocrystallites becomes larger.

In order to estimate the nanocrystallite sizes, we have calculated the average distance between the minimums on the profiles shown in Figure 2A. Assuming compact packing of the spherical nanocrystallites this distance should correspond to the size of a single nanocrystallite. The sizes of the nanocrystallites estimated from the profiles given in Figure 2A have been found to be  $97 \pm 27$ ,  $140 \pm 47$ , and  $221 \pm 65$  nm in diameter for crystals prepared at 7.5, 22, and 45 °C, respectively. The pore size of the crystals can be estimated as a diameter of a sphere placed in a free space between compactly packed nanocrystallites (assumed to be spherical). Simple mathematical calculations show that this diameter is about 20% of the size of nanocrystallites. Thus, the estimated pore sizes were found to be  $19 \pm 5$ ,  $28 \pm 9$ , and  $44 \pm 13$  nm for crystals prepared at 7.5, 22, and 45 °C, respectively.

To compare the porosity of the crystals, the specific surface area and pore size have been measured by nitrogen adsorption–desorption using the BET approach. Typical isotherms are shown in Figure S2. For the crystals prepared at 22 and 45 °C, the surface area was 17.5 and 10.5  $\text{m}^2/\text{g}$ , respectively. The pore size for the crystals was found to be in the range 5–20 nm, and the average size of the prepared crystals is about 10 and 15 nm, respectively (Figure S3). The decrease of the specific surface area and pore size are related to the decrease of surface-to-volume ratio for larger nanocrystallites formed at a higher temperature. XRD has been employed to calculate the average size of the nanocrystallites, and it was found to be 63 and 93 nm for the crystals prepared at 22 and 45 °C, respectively (Table S1). Thus, the SEM analysis shows overestimated results of sizes of the nano-

crystallites and pores; however, the trend in the sizes as a function of the preparation temperature is the same. XRD has also shown that the most of the crystals belong to vaterite form of calcium carbonate (Figure S4); only 14 and 9% of calcite have been revealed in the samples prepared at 45 and 25 °C, respectively.

To prove that the observed morphological changes of the crystal surface result from variation of the preparation temperature, it is necessary to analyze the internal structure of the crystals. First we have examined the internal crystal structure by identification of the  $\text{CaCO}_3$  polymorph form. Raman microspectroscopy has revealed that the prepared crystals belong to the vaterite form of  $\text{CaCO}_3$  (Figure 2B); it is concluded from the typical bands of the vaterite described in literature.<sup>50–52</sup> No calcite has been found when analyzing single spherical crystals. This gives the first evidence that the crystals are fully porous and composed of nanocrystallites, which is typical for the vaterite polymorph form. SEM images of the broken  $\text{CaCO}_3$  crystal confirm the porous nature of the internal crystal structure (Figure 2C). AFM has been employed to further analyze the crystal internal structure. AFM has been used for analysis of both the surface and the internal structure of the crystals. Figure 3A–C shows AFM images of the crystals prepared at varied temperatures, 7.5, 22, and 45 °C. The crystal surface texture is similar to that observed by SEM analysis, and rather spherical nanocrystallites can be identified from 2D and 3D images. The profiles taken from the AFM images show that the height and width of the nanocrystallites are increased with an increase of the crystal preparation temperature. This is the same trend observed by analysis of the SEM images (Figures 1 and 2A). The average roughness of the crystal surfaces has increased with the temperature rise too. Root mean square

roughness values were found to be 6.3, 12.6, and 16.1 nm for the crystal preparation temperatures of 7.5, 22, and 45 °C, respectively. Thus, morphological analysis of the crystal surface by SEM and AFM has revealed similar trends as BET and XRD results as well.

In order to find a correlation between the texture of the crystal surface and its interior, the crystals (prepared at 7.5 °C) have been mechanically broken and the crystal internal part has been analyzed. The morphology of the broken particle has shown to be less regular as compared to the morphology of the surface of unbroken crystal (Figure 3A,D). The features on the surface of the unbroken crystal (Figure 3A) are in dimensions of 15 nm as can be concluded from the profile to be a representative image. The same dimensions are typical for the broken crystal (Figures 3D and S5); however, one can clearly see a few cavities in the texture of the broken crystal (Figure 3D, indicated by red arrows). These cavities might be caused by the breaking process. Thus, the surface texture of the crystals is similar to the internal morphology of the crystal; however, one should be aware that some artifacts may be observed due to the breakage. For even more reliable study, one should cut the crystal without the breakage of the nanocrystallites; however, this is complicated due to hard nature of the calcium carbonate.

To better examine the internal crystal structure, we have studied the permeability of macromolecules through the pores, a technique that reflects pore sizes. Uncharged dextran-FITC has been employed to minimize an interaction of the permeating molecules with the carbonate surface that may reduce molecular diffusion into the pores or even fully prevent it by blocking the pores on a crystal edge. Figures S6 and S7 show CLSM images of the crystals prepared at 22 and 45 °C in the presence of dextran-FITC of 10 and 70 kDa (hydrodynamic diameters 3.8 and 13 nm, respectively<sup>53</sup>). Both crystal types are permeable for 10 kDa dextran, meaning that the pore size is above 3.8 nm. However, 70 kDa dextran cannot diffuse into the crystals prepared at 22 °C but can diffuse into those prepared at 45 °C. Thus, from the results presented in Figures S6 and S7, one can conclude that the porosity of crystals prepared at 22 and 45 °C is different. Diffusion limitations for the 13 nm sized dextran are observed for particles prepared at 22 °C. This is expected because the average estimated size of the pores for these particles is about 28 nm as described above that may lead to restrictions of dextran molecules to freely diffuse into the pores. Permeability studies allow one to define a cutoff for the macromolecular diffusion through the pores of the CaCO<sub>3</sub> crystals. Here, the crystals prepared at 22 and 45 °C have respective cutoff sizes in the range 3.8–13 and above 13 nm. It is of note that the dextran molecules diffused into the crystals are found in the whole crystal volume (Figures S6 and S7). Some rather smooth and cupola-like distribution of dextrans may be related to optical effects on the crystal surface due to higher reflective index of calcium carbonate if compared to water. The presentation of the dextran molecules inside the whole crystal points to a rather uniform internal structure of the crystals.

**The Mechanism of CaCO<sub>3</sub> Crystal Growth.** The observed effect of temperature on the structure of the vaterite crystals may be explained by considering the mechanism of the vaterite crystallization. Vaterite crystals are usually (as in this study) prepared at conditions of supersaturation in respect to initial salts, here CaCl<sub>2</sub> and Na<sub>2</sub>CO<sub>3</sub>. Mixing of the salts results in a formation of so-called amorphous calcium carbonate (ACC) which further transforms into vaterite crystals. Recently,

the growth of vaterite CaCO<sub>3</sub> crystals has been explicitly studied,<sup>48</sup> revealing the spherulitic growth.<sup>46,48,54</sup> According to that study,<sup>48</sup> the growth takes place in two main steps: (i) ACC dehydration followed by transformation of primary vaterite crystals to growth, and (ii) surface-mediated Ostwald ripening of the formed vaterite crystals. Vaterite crystals have a secondary structure and are thus called polycrystallites. They are composed of nanocrystallites which have a size in the range of nanometers. The spherulitic growth described in ref 48 has been adopted for interpretation of the results of this study. Schematic presentation of the proposed crystal growth mechanism is given in Figure 4. In the first step, the primary

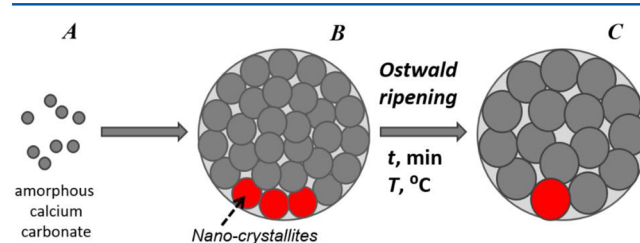


**Figure 4.** Scheme of the proposed mechanism of vaterite crystal growth. Primary vaterite crystals (B) are formed by amorphous calcium carbonate dehydration (A,B). Ostwald ripening results in the growth of nanocrystallines while keeping the size of the vaterite crystal unaffected (B,C).

vaterite crystals are formed from ACC (Figure 4A,B). At near equilibrium saturation conditions, the vaterite crystals are fully formulated and the most of ACC is consumed (Figure 4B). However, the internal structure of the crystals is changing over time through Ostwald ripening of the small nanocrystallites stuck to each other (Figure 4B,C). Larger nanocrystallites grow by dissolution of smaller ones due to a reduction of the total contact area with a solvent. This leads to a decrease of the surface energy, and is favorable from a thermodynamic point of view. During the nanocrystallite growth the size of the nanocrystallites is increased from 9 to 37 nm after growth time of 30 min.<sup>48</sup> In our results, the estimated size of the nanocrystallites from SEM and AFM images (crystal growth at 22 °C) is larger, about 140 nm. This might be due to longer growth time (80 min instead of 30 min) that results in a progressive growth of the nanocrystallites.

The temperature-mediated control over the crystal porosity observed here can be explained by the growth mechanism described above. Since an increase of temperature leads to an increase of a rate of any chemical reaction, the Ostwald ripening will take place faster at higher preparation temperature (Figure 4B,C). Thus, for the same period of time (crystal growth time), the nanocrystallites will be larger for crystals prepared at higher temperatures. Temperature variation during the vaterite crystal growth gives an easy way to control the crystal porosity without any additives.

**Design of Hollow and Matrix-Type Polyelectrolyte Microcapsules.** Control over internal structure of the vaterite crystals is indispensable for designing polymer microparticles assembled by hard templating using these crystals. To demonstrate design of the polymer architectures templated by the CaCO<sub>3</sub> crystals, we have prepared polyelectrolyte capsules by the LbL technique using the crystals synthesized at different temperatures: 22 and 45 °C. Microcapsules made of PAH and PSS have been assembled using the established protocol<sup>7</sup> using PAH-FITC to monitor the distribution of the

polyelectrolytes in the formed capsules (Figure 5). The schematics of the capsule fabrication is given in Figure 6 and

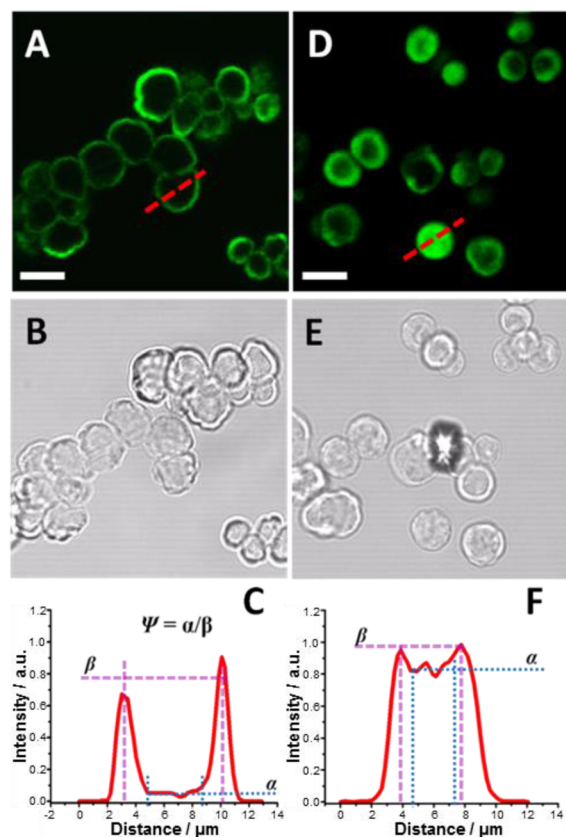


**Figure 5.** CLSM images of (PAH/PSS)<sub>6</sub> microcapsules prepared using CaCO<sub>3</sub> crystals made at 22 °C (A, B) and at 45 °C (D, E). Panels (C) and (F) represent fluorescent profiles of the capsules depicted in the images (A) and (D), respectively. The  $\Psi$  value has been calculated as a ratio of  $\alpha$  to  $\beta$ ; for more details, see the main text. Scale bar is 10  $\mu$ m.

includes coating of the crystals with multilayer shell followed by elimination of the crystals in EDTA. CLSM images of the fabricated (PAH/PSS)<sub>6</sub> capsules demonstrate that shell-like capsules (polymers are mostly on the capsule edges) and matrix-type capsules (polymers are distributed inside the capsule) are formed using the crystals prepared at 22 and at

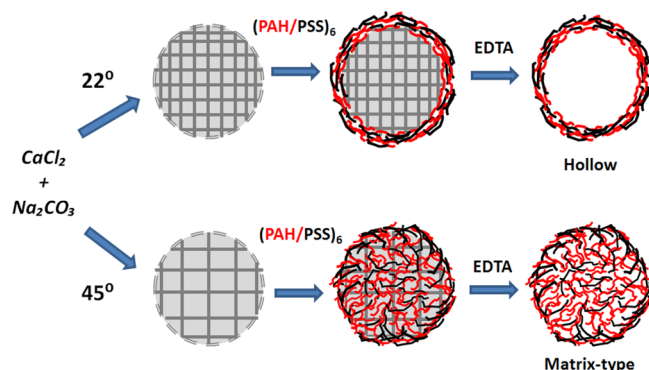


**Figure 6.** Scheme of capsule fabrication and encapsulation of macromolecules into capsules at different temperature (22 and 45 °C). Upper and bottom parts show the sequence of assembly of hollow and matrix-like capsules, respectively.

45 °C, respectively (Figure 5). Since some variations in the polymer distribution in the capsules have been observed, we have performed a more detailed analysis of the polymer distribution in the capsules. CLSM profiles (Figure 5C and F) have been treated to obtain an average value  $\psi$  which reflects the polymer distribution in the capsules.  $\psi$  has been calculated as the ratio of  $\alpha$  to  $\beta$  as shown in Figure 5C and F.  $\alpha$  represents a measure of a fluorescent signal coming from the capsule interior. It is defined as a mean fluorescence in the middle third of the profile.  $\beta$  is defined as half of a mean fluorescence of the capsule edges. Thus, the more polymer is in the capsule interior, the higher is the  $\psi$  value. For  $\psi$  equal to one, the capsule should be “filled” with polymers to a half, if the capsule consists of uniformly distributed polymer molecules, the  $\psi$  value should be 2.  $\psi$  values for the capsules prepared on the crystals grown at 22 and at 45 °C were found to be  $0.47 \pm 0.13$  and  $1.24 \pm 0.43$ , respectively. It is clear that the capsules with more polymers inside will be assembled on the crystals with larger pores (crystals prepared at 45 °C). This is due to more pronounced polymer diffusion through the larger pores. Thus, the design of the polymer particles templated on the vaterite CaCO<sub>3</sub> crystals with controlled porosity is possible. The capsule structure observed cannot be associated with incomplete elimination of the crystals because the only slight trace amount (below 0.1% by weight) of calcium carbonate is found the formed capsules.<sup>7</sup>

Schematic representation of the matrix- and shell-type capsule formation (Figure 6) can be drawn based on the experimental results described above. The hydrodynamic diameter of PSS and PAH (both 70 kDa) should be in the range of 10–15 nm at low ionic strength used in this study.<sup>55,56</sup> The size of the polyelectrolytes corresponds well to the size of dextran 70 kDa (13 nm) which has diffusion limitation for crystals made at 22 °C. Therefore, the pore-dependent permeation of the polyelectrolyte (PSS and PAH) is expected and proven by the experiment. In general, most polymers including biopolymers (proteins, peptides, enzymes, nucleic acids, and growth factors) have sizes from a few nanometers up to a few tens of nanometers. This corresponds to the molecular mass of them typically lying in the range from a few kDa up to hundreds kDa. Such sizes are in the range of the pore size of the CaCO<sub>3</sub> crystals prepared here at different temperatures. Thus, the control over the mesoporous structure of the crystals can govern biomolecule permeation/distribution into the crystals. This gives an option to design biomolecule containing particles by means of CaCO<sub>3</sub>-based templating.

**Modeling of the CaCO<sub>3</sub> Crystal Internal Structure.** In the last part of this study, we have estimated the accessibility of molecules to internal volume of the porous CaCO<sub>3</sub> microcrystals. For this purpose geometrical calculations have been made assuming that the microcrystal is composed from closely packed spherical nanocrystallites of radius  $r$  as shown in Figure 7A. If several equal-sized layers of nanocrystallites are added, the resulting microparticle is a parallelepiped. The form of this parallelepiped differs from spherical microparticles known from the experiments. Nevertheless, the resulting dependencies, like the dependency between microparticle surface and the nanocrystallite radius, will be qualitatively correctly described by a parallelepiped model. This is expected at least if volume effects are more dominant than surface effects, or in other words if the diameter of the nanocrystallites is small compared with dimension of the microparticle (this is the case for the CaCO<sub>3</sub> microcrystals).

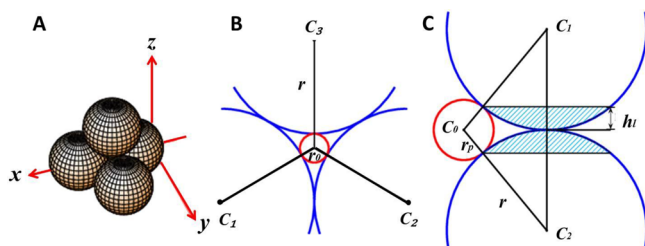


**Figure 7.** (A) Schematic showing closely packed spherical nanocrystallites of radius  $r$ . (B) Cross section of three closely packed nanocrystallites (in blue); red circle represents the largest molecule which can access the free volume between the nanocrystallites. (C) Cross section of two nanocrystallites being in contact and the surface (light blue lines) of the nanocrystallites which is not available for the adsorbed molecule (the molecule is the red circle).

On the other hand, it is possible to handle the parallelepiped in an analytical way, while it is almost impossible to do this with a spherical microparticle. This can be done only with numerical methods. Thus, the following analytical considerations should characterize some typical dependencies of microparticle properties on nanocrystallite parameters.

First, we have focused on the relation between the size of the nanocrystallites and the total surface area of the  $\text{CaCO}_3$  microcrystals. The surface  $S_{\mu\text{C}}^{\text{spheres}}$  of the  $n^3$  spheres (nanocrystallites) in a regular parallelepiped with  $n$  spheres along all edges is

$$S_{\mu\text{C}}^{\text{spheres}}(n, r) = 4n^3\pi r^2 \quad (1)$$

The volume of the corresponding enveloping parallelepiped is

$$V_{\text{pe}} = 4\sqrt{2}r^3(n_s + n)^3 = \frac{l_{\text{pe}}^3}{\sqrt{2}} \quad (2)$$

where  $l_{\text{pe}}$  is the edge length of the parallelepiped and

$$n_s = \frac{\sqrt{6}}{2} - 1 \approx 0.225 \dots \quad (3)$$

The surface of the parallelepiped is

$$A_{\text{pe}} = 12\sqrt{3}r^2(n_s + n)^2 = 3\sqrt{3}l_{\text{pe}}^2 \quad (4)$$

The surface of  $n^3$  nanocrystallites as a function of the nanocrystallite radius for a fixed parallelepiped edge length  $l_{\text{pe}}$  can be expressed as

$$S_{\text{spheres}}(l_{\text{pe}}, r) = \frac{\pi}{2r}[l_{\text{pe}} - 2rn_s]^3 \quad (5)$$

Equations 3–5 and the following equations make sense only if there is at least one nanocrystallite. This corresponds to a maximal radius  $r_{\text{max}}$ :

$$r_{\text{max}} = \frac{l_{\text{pe}}}{2(1 - n_s)} \quad (6)$$

If on the other hand, the nanocrystallite radius is relatively small, i.e., if

$$\frac{l_{\text{pe}}}{2r} > 3n_s \approx 0.674 \dots \quad (7)$$

The last term in the brackets of eq 5 can be neglected, and the total surface of all nanocrystallites is proportional to the reciprocal radius:

$$S_{\text{spheres}}(l_{\text{pe}}, r) \approx \pi \frac{l_{\text{pe}}^3}{2r} \quad (8)$$

Let us again consider the crystal growth mechanism (Figure 4). The surface and the volume of the crystal during Ostwald ripening is kept the same (Figure 4), just the nanocrystallites are enlarged, decreasing the total crystal surface area. The relation between the total surface  $S$  and the size of the nanocrystallite of radius  $r$  is of particular interest. According to eq 8, the ratio between the total surface  $S_1$  and  $S_2$  of the crystal during its growth at time  $t_1$  and  $t_2$  will be inversely proportional to the ratio between the nanocrystallite radii  $r_1$  and  $r_2$  at these moments in time:

$$\frac{S_{\text{spheres}}(l_{\text{pe}}, r_2)}{S_{\text{spheres}}(l_{\text{pe}}, r_1)} = \frac{r_1}{r_2} \quad (9)$$

Thus, the surface area calculated for the crystals at a certain moment of its growth (or growth at different temperature) can be used to estimate the difference between sizes of the nanocrystallites. As mentioned above, BET experiments have shown that the ratio of surface area and sample mass of the crystals prepared at 22 and 45 °C was found to be 17 and 11  $\text{m}^2/\text{g}$ , respectively. The ratio between the surface areas of the crystals prepared at 22 and 45 °C is 1.55. The diameters of the nanocrystallites estimated from the profiles given in Figure 2A have been found to be  $140 \pm 47$  and  $221 \pm 65$  nm for crystals prepared at 22 and 45 °C, respectively. The ratio between the sizes is 1.58, very close to the predicted value according to the eq 9.

In the next step the accessibility of molecules to internal volume of the porous  $\text{CaCO}_3$  microcrystals has been examined. Figure 7B presents the scheme showing cross sections of three spherical close-packed nanocrystallites (in blue) of radius  $r$  and the red circle representing the largest molecule which can access the free volume between the nanocrystallites. The size of this molecule (radius  $r_0$ ) will determine a cutoff for molecular diffusion into the porous  $\text{CaCO}_3$  crystals. eq 10 shows a relation between the radii  $r$  and  $r_0$ :

$$r_0 = r \frac{2\sqrt{3} - 3}{3} \approx 0.155 \dots r \quad (10)$$

As can be concluded from the equation above, the size of the largest molecule which can access the free volume of the  $\text{CaCO}_3$  crystals is about 15% of the size of the nanocrystallites. Thus, the crystals with smallest pore size (crystals prepared at 7.5 °C have nanocrystallites of  $97 \pm 27$  nm in diameter) are permeable for the majority of macromolecules because the cutoff will be about 15 nm; close to the size of very large proteins such as catalase (250 kDa, 11 nm in diameter<sup>57</sup>). The  $\text{CaCO}_3$  crystals with larger pores (prepared at 22 or 45 °C) will be even more penetrable for molecules of interest.

Figure 7C shows a cross section of two spherical nanocrystallites (in blue) and the surface of the nanocrystallites which is not accessible to the adsorbed molecule (the molecule is the red circle). The number of contact points of  $n^3$  nanocrystallites in the polycrystal is

$$N_n^{\text{C}} = 6n^3 - 9n^2 + 3n \quad (11)$$

The surface of the spherical layer with the height ( $h_1$ ) of one nanocrystallite without the area of the plane circle can be calculated to compare with Figure 7C:

$$S_{\text{SL}} = 2\pi r h_1 = 2\pi \frac{r^2 r_p}{r_p + r} \quad (12)$$

The surface area at one contact point of a nanocrystallite which is not accessible by a “spherical liquid” molecule with a radius  $r_p$  is then  $2S_{\text{SL}}$ . For the total accessible surface of the whole parallelepiped, the area for  $2N_n^C$  contact layers has to be subtracted from the total surface area of all nanocrystallites (eq 1), resulting:

$$S_{\text{spheres}}^{\text{accessible}}(n, r) = 4\pi r^2 n^3 \left\{ 1 - 3 \left[ 2 - \frac{3}{n} + \frac{1}{n^2} \right] \frac{r_p}{r_p + r} \right\} \quad (13)$$

which can be also expressed for a fixed volume of the parallelepiped (polycrystal) with the edge length  $l_{\text{pe}}$  for  $r_0 < r < r_{\text{max}}$  as

$$S_{\text{spheres}}^{\text{accessible}}(l_{\text{pe}}, r) = \frac{\pi}{r} (l_{\text{pe}} - 2n_s r)^3 \times \left\{ 1 - 3 \left[ 2 - \frac{6r}{l_{\text{pe}} - 2rn_s} + \frac{4r^2}{(l_{\text{pe}} - 2rn_s)^2} \right] \frac{r_p}{r_p + r} \right\} \quad (14)$$

For  $r \leq r_0$ , only the external surface of microparticle is accessible, which can be estimated roughly as the surface area of the parallelepiped  $A_{\text{pe}}$  (eq 4). Equation 14 can be used to estimate surface area ( $S_{\text{spheres}}^{\text{accessible}}$ ) of the crystal of external volume  $V$  accessible for the adsorbed molecule of radius  $r_p$  if the radius of the nanocrystallites is  $r$ . Based on these relations, one can calculate the accessible surface area of the porous  $\text{CaCO}_3$  crystals (the edge length  $l_{\text{pe}}$  of the parallelepiped is taken as 10  $\mu\text{m}$ , corresponding to  $l_{\text{pe}} = 10 \mu\text{m}$ , a volume  $V_{\text{pe}}$  of 707.1  $\mu\text{m}^3$ . The results are shown in Figure 8.

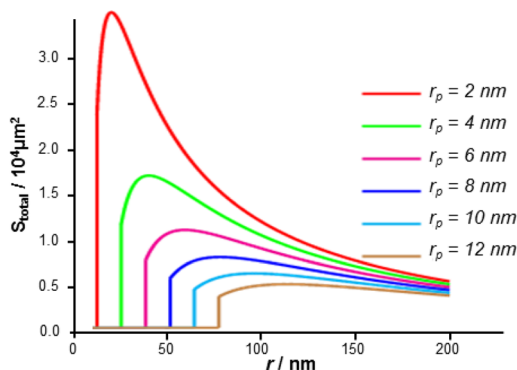


**Figure 8.** Calculated accessible surface as a function of nanocrystallite radius for the adsorbents of radii  $r_p$ .

If the nanocrystallite radius  $r$  is taken to be 100 nm, and some adsorbents with radii 12, 10, 8, 6, and 4 nm would be used to measure the accessible surface, it is shown that the surface is increasing with decreasing adsorbent radius. This is due to the decrease of nonaccessible area around the contact points of the nanocrystallites with decreasing adsorbent radius. If the same would be tested with nanocrystallites with 50 nm radii, the result differs a little. Decreasing the adsorbent radius from 12 to 8 nm, the accessible surface stays almost constant at the value of the surface of the parallelepiped, because the adsorbent is too large to penetrate the microparticle. If the size

of the adsorbent is decreased under 8 nm, the same behavior as before is shown. Alternatively, experiments can be run with a series of differently sized nanocrystallites with a fixed adsorbent size (e.g.,  $r_p = 8$  nm). Starting with nanosphere size of 10 nm, the amount of adsorbent bound to the microparticle should not change until the nanospheres reach 50 nm. Only the external surface of the microparticle is accessible, if the size of nanocrystallite is further increased the pores become so large, that the 8 nm adsorbent molecule can enter the polycrystallite cavities and the accessible surface is increased. If the size of the nanocrystallite is further increased over 60 nm, the cavities are further enlarged, but the number of cavities is reduced, which results again in decreasing the accessible surface.

These molecules include solvents such as water (0.15 nm), rather small proteins or peptides (3 nm), large biomacromolecules (30 nm) such as protein fibronectin, or other biologically relevant large proteins as well as very large molecules (300 nm) with diameters exceeding the pore size. The diameters of the molecules are assumed to be different from each other and to be close to typical dimensions of these molecules. As shown in Figure 8, small molecules such as water can occupy a much higher surface area if compared to larger molecules with diameters of 3 or 30 nm.

We believe that control over porosity of the  $\text{CaCO}_3$  vaterite crystals will open new perspectives for template-assisted design of polymer particles with tailor-made structures. This should first of all include the templated particles containing bioactive molecules due to mild decomposition conditions as a significant advantage of the  $\text{CaCO}_3$  crystals for hard templating. Coprecipitation or cosynthesis approach<sup>28–32</sup> may also be considered for control over the crystal porosity by addition of the molecules of interest during crystal preparation. This would allow one to both include the molecules into the crystals and adjust crystal pore size at the same time. These aspects are to be considered in our future research. We also would like to utilize the  $\text{CaCO}_3$  crystals with adjusted porosity for the crystal assisted templating of capsule-<sup>58</sup> and alginate-based<sup>59,60</sup> polymeric scaffolds offering controlled loading and release of bioactive molecules to cells seeded into the scaffolds. Design of such functional biomaterials of challenging for tissue engineering and regenerative medicine. The knowledge in tuning of the multilayer properties by as well as loading of the multilayers with biomolecules would be beneficial.<sup>61–63</sup>

## CONCLUSIONS

In this work, we have shown that the porosity of vaterite  $\text{CaCO}_3$  crystals can be adjusted by variation of preparation temperature for crystal preparation at supersaturated conditions. Surface morphology of the crystals reflects the internal structure of the crystals as found by permeability study using uncharged dextrans. The internal structure is rather homogeneous within one crystal but deviations in porosity between the crystals are observed. The effect of preparation temperature on the crystal internal structure can be explained by spherulitic growth accompanied by Ostwald ripening of the nanocrystallites stuck to each other forming the  $\text{CaCO}_3$  crystal. According to this, the growth rate of the nanocrystallites should depend on temperature, leading to larger nanocrystallites formed at higher preparation temperature. Finally, the crystals with different porosity can be used to prepare polyelectrolyte capsules of defined structure: matrix-type capsules for crystals with larger pores and shell-type capsules for the crystals with

smaller pores. This corresponds to deeper or restricted polymer diffusion into the crystal, respectively.

## ■ ASSOCIATED CONTENT

### ● Supporting Information

The Supporting Information is available free of charge on the ACS Publications website at DOI: 10.1021/acs.langmuir.6b00717.

Additional SEM images of the crystals, nitrogen sorption isotherms, crystal pore size distribution, crystal X-ray diffraction patterns, CLSM images of the crystals in the presence of dextran-FITC, and additional AFM images of a broken crystal (PDF)

## ■ AUTHOR INFORMATION

### Author Contributions

The manuscript was written through contributions of all authors. All authors have given approval to the final version of the manuscript.

### Notes

The authors declare no competing financial interest.

## ■ ACKNOWLEDGMENTS

This work was supported by the Alexander von Humboldt Foundation (Sofja Kovalevskaja program). The authors thank Rona Pitschke and Heike Runge for SEM imaging.

## ■ REFERENCES

- (1) Ariga, K.; Hill, J. P.; Ji, Q. Layer-by-layer assembly as a versatile bottom-up nanofabrication technique for exploratory research and realistic application. *Phys. Chem. Chem. Phys.* **2007**, *9*, 2319–2340.
- (2) Ariga, K.; Ji, Q. M.; Hill, J. P.; Vinu, A. Coupling of soft technology (layer-by-layer assembly) with hard materials (mesoporous solids) to give hierarchic functional structures. *Soft Matter* **2009**, *5*, 3562–3571.
- (3) Estroff, L. A.; Hamilton, A. D. At the interface of organic and inorganic chemistry: Bioinspired synthesis of composite materials. *Chem. Mater.* **2001**, *13*, 3227–3235.
- (4) Thomas, A.; Goettmann, F.; Antonietti, M. Hard Templates for Soft Materials: Creating Nanostructured Organic Materials†. *Chem. Mater.* **2008**, *20*, 738–755.
- (5) Huczko, A. Template-based synthesis of nanomaterials. *Appl. Phys. A: Mater. Sci. Process.* **2000**, *70*, 365–376.
- (6) Caruso, F.; Caruso, R. A.; Mohwald, H. Nanoengineering of inorganic and hybrid hollow spheres by colloidal templating. *Science* **1998**, *282*, 1111–1114.
- (7) Volodkin, D. V.; Petrov, A. I.; Prevot, M.; Sukhorukov, G. B. Matrix Polyelectrolyte Microcapsules: New System for Macromolecule Encapsulation. *Langmuir* **2004**, *20*, 3398–3406.
- (8) Schmidt, S.; Volodkin, D. Microparticulate biomolecules by mild CaCO<sub>3</sub> templating. *J. Mater. Chem. B* **2013**, *1*, 1210–1218.
- (9) Volodkin, D. CaCO<sub>3</sub> templated micro-beads and -capsules for bioapplications. *Adv. Colloid Interface Sci.* **2014**, *207*, 306–324.
- (10) Dellacasa, E.; Zhao, L.; Yang, G. S.; Pastorino, L.; Sukhorukov, G. B. Fabrication and characterization of novel multilayered structures by stereocomplexation of poly(D-lactic acid)/poly(L-lactic acid) and self-assembly of polyelectrolytes. *Beilstein J. Nanotechnol.* **2016**, *7*, 81–90.
- (11) Kakran, M.; Muratani, M.; Tng, W. J.; Liang, H. Q.; Trushina, D. B.; Sukhorukov, G. B.; Ng, H. H.; Antipina, M. N. Layered polymeric capsules inhibiting the activity of RNases for intracellular delivery of messenger RNA. *J. Mater. Chem. B* **2015**, *3*, 5842–5848.
- (12) Behra, M.; Schmidt, S.; Hartmann, J.; Volodkin, D. V.; Hartmann, L. Synthesis of Porous PEG Microgels Using CaCO<sub>3</sub>-Microspheres as Hard Templates. *Macromol. Rapid Commun.* **2012**, *33*, 1049–1054.
- (13) Gao, C. Y.; Moya, S.; Lichtenfeld, H.; Casoli, A.; Fiedler, H.; Donath, E.; Mohwald, H. The decomposition process of melamine formaldehyde cores: the key step in the fabrication of ultrathin polyelectrolyte multilayer capsules. *Macromol. Mater. Eng.* **2001**, *286*, 355–361.
- (14) Balabushevich, N. G.; Tiourina, O. P.; Volodkin, D. V.; Larionova, N. I.; Sukhorukov, G. B. Loading the Multilayer Dextran Sulfate/Protamine Microsized Capsules with Peroxidase. *Biomacromolecules* **2003**, *4*, 1191–1197.
- (15) Wang, Y.; Yu, A.; Caruso, F. Nanoporous Polyelectrolyte Spheres Prepared by Sequentially Coating Sacrificial Mesoporous Silica Spheres. *Angew. Chem., Int. Ed.* **2005**, *44*, 2888–2892.
- (16) Tan, J.; Wang, Y.; Yip, X.; Glynn, F.; Shepherd, R. K.; Caruso, F. Nanoporous Peptide Particles for Encapsulating and Releasing Neurotrophic Factors in an Animal Model of Neurodegeneration. *Adv. Mater.* **2012**, *24*, 3362–3366.
- (17) Wang, Y. J.; Caruso, F. Nanoporous protein particles through templating mesoporous silica spheres. *Adv. Mater.* **2006**, *18*, 795–800.
- (18) Shenoy, D. B.; Antipov, A. A.; Sukhorukov, G. B.; Mohwald, H. Layer-by-Layer Engineering of Biocompatible, Decomposable Core–Shell. *Biomacromolecules* **2003**, *4*, 265–272.
- (19) Volodkin, D. V.; Schmidt, S.; Fernandes, P.; Larionova, N. I.; Sukhorukov, G. B.; Duschl, C.; Möhwald, H.; von Klitzing, R. One-Step Formulation of Protein Microparticles with Tailored Properties: Hard Templating at Soft Conditions. *Adv. Funct. Mater.* **2012**, *22*, 1914–1922.
- (20) Parakhonskiy, B. V.; Haase, A.; Antolini, R. Sub-Micrometer Vaterite Containers: Synthesis, Substance Loading, and Release. *Angew. Chem., Int. Ed.* **2012**, *51*, 1195–1197.
- (21) Parakhonskiy, B. V.; Yashchenok, A. M.; Donatan, S.; Volodkin, D. V.; Tessarolo, F.; Antolini, R.; Mohwald, H.; Skirtach, A. G. Macromolecule Loading into Spherical, Elliptical, Star-Like and Cubic Calcium Carbonate Carriers. *ChemPhysChem* **2014**, *15*, 2817–2822.
- (22) De Temmerman, M.-L.; Demeester, J.; De Vos, F.; De Smedt, S. C. Encapsulation Performance of Layer-by-Layer Microcapsules for Proteins. *Biomacromolecules* **2011**, *12*, 1283–1289.
- (23) Volodkin, D. V.; von Klitzing, R.; Möhwald, H. Pure Protein Microspheres by Calcium Carbonate Templating. *Angew. Chem., Int. Ed.* **2010**, *49*, 9258–9261.
- (24) Wang, C.; He, C.; Tong, Z.; Liu, X.; Ren, B.; Zeng, F. Combination of adsorption by porous CaCO<sub>3</sub> microparticles and encapsulation by polyelectrolyte multilayer films for sustained drug delivery. *Int. J. Pharm.* **2006**, *308*, 160–167.
- (25) Schmidt, S.; Behra, M.; Uhlir, K.; Madaboosi, N.; Hartmann, L.; Duschl, C.; Volodkin, D. Mesoporous Protein Particles Through Colloidal CaCO<sub>3</sub> Templates. *Adv. Funct. Mater.* **2013**, *23*, 116–123.
- (26) Fujii, A.; Maruyama, T.; Ohmukai, Y.; Kamio, E.; Sotani, T.; Matsuyama, H. Cross-linked DNA capsules templated on porous calcium carbonate microparticles. *Colloids Surf., A* **2010**, *356*, 126–133.
- (27) Yan, X. H.; Li, J. B.; Mohwald, H. Templating Assembly of Multifunctional Hybrid Colloidal Spheres. *Adv. Mater.* **2012**, *24*, 2663–2667.
- (28) Petrov, A. I.; Volodkin, D. V.; Sukhorukov, G. B. Protein-calcium carbonate co-precipitation. A tool for protein encapsulation. *Biotechnol. Prog.* **2005**, *21*, 918–925.
- (29) Mak, W. C.; Georgieva, R.; Renneberg, R.; Baumler, H. Protein Particles Formed by Protein Activation and Spontaneous Self-Assembly. *Adv. Funct. Mater.* **2010**, *20*, 4139–4144.
- (30) He, G.; He, Z. To prepared fluorescent chitosan capsules by in situ polyelectrolyte coacervation on poly(methacrylic acid)-doped porous calcium carbonate microparticles. *Polym. Bull.* **2012**, *69*, 263–271.
- (31) Kurapati, R.; Raichur, A. M. Composite cyclodextrin-calcium carbonate porous microparticles and modified multilayer capsules: novel carriers for encapsulation of hydrophobic drugs. *J. Mater. Chem. B* **2013**, *1*, 3175–3184.

- (32) Kreft, O.; Prevot, M.; Möhwald, H.; Sukhorukov, G. B. Shell-in-Shell Microcapsules: A Novel Tool for Integrated, Spatially Confined Enzymatic Reactions. *Angew. Chem., Int. Ed.* **2007**, *46*, 5605–5608.
- (33) Volodkin, D. V.; Larionova, N. I.; Sukhorukov, G. B. Protein Encapsulation via Porous CaCO<sub>3</sub> Microparticles Templating. *Bio-macromolecules* **2004**, *5*, 1962–1972.
- (34) Peng, C.; Zhao, Q.; Gao, C. Sustained delivery of doxorubicin by porous CaCO<sub>3</sub> and chitosan/alginate multilayers-coated CaCO<sub>3</sub> microparticles. *Colloids Surf., A* **2010**, *353*, 132–139.
- (35) De Koker, S.; De Cock, L. J.; Rivera-Gil, P.; Parak, W. J.; Velty, R. A.; Vervaet, C.; Remon, J. P.; Grooten, J.; De Geest, B. G. Polymeric multilayer capsules delivering biotherapeutics. *Adv. Drug Delivery Rev.* **2011**, *63*, 748–761.
- (36) Vogel, R.; Persson, M.; Feng, C.; Parkin, S. J.; Nieminen, T. A.; Wood, B.; Heckenberg, N. R.; Rubinsztein-Dunlop, H. Synthesis and Surface Modification of Birefringent Vaterite Microspheres. *Langmuir* **2009**, *25*, 11672–11679.
- (37) Cölfen, H. Precipitation of carbonates: recent progress in controlled production of complex shapes. *Curr. Opin. Colloid Interface Sci.* **2003**, *8*, 23–31.
- (38) Tong, H.; Ma, W.; Wang, L.; Wan, P.; Hu, J.; Cao, L. Control over the crystal phase, shape, size and aggregation of calcium carbonate via a l-aspartic acid inducing process. *Biomaterials* **2004**, *25*, 3923–3929.
- (39) Naka, K.; Chujo, Y. Control of Crystal Nucleation and Growth of Calcium Carbonate by Synthetic Substrates. *Chem. Mater.* **2001**, *13*, 3245–3259.
- (40) Kitamura, M. Crystallization and Transformation Mechanism of Calcium Carbonate Polymorphs and the Effect of Magnesium Ion. *J. Colloid Interface Sci.* **2001**, *236*, 318–327.
- (41) Meldrum, F. C.; Hyde, S. T. Morphological influence of magnesium and organic additives on the precipitation of calcite. *J. Cryst. Growth* **2001**, *231*, 544–558.
- (42) Guo, J. H.; Severtson, S. J. Application of classical nucleation theory to characterize the influence of carboxylate-containing additives on CaCO<sub>3</sub> nucleation at high temperature, pH, and ionic strength. *Ind. Eng. Chem. Res.* **2003**, *42*, 3480–3486.
- (43) Agarwal, P.; Berglund, K. A. Effect of polymeric additives on calcium carbonate crystallization as monitored by nephelometry. *Cryst. Growth Des.* **2004**, *4*, 479–483.
- (44) Guo, X. H.; Liu, L.; Wang, W.; Zhang, J.; Wang, Y. Y.; Yu, S. H. Controlled crystallization of hierarchical and porous calcium carbonate crystals using polypeptide type block copolymer as crystal growth modifier in a mixed solution. *CrystEngComm* **2011**, *13*, 2054–2061.
- (45) Nakamura, S.; Naka, K. Size-Controlled Vaterite Composite Particles with a POSS-Core Dendrimer for the Fabrication of Calcite Thin Films by Phase Transition. *Langmuir* **2013**, *29*, 15888–15897.
- (46) Beck, R.; Andreassen, J.-P. The onset of spherulitic growth in crystallization of calcium carbonate. *J. Cryst. Growth* **2010**, *312*, 2226–2238.
- (47) Yamanaka, S.; Oiso, T.; Kurahashi, Y.; Abe, H.; Hara, K.; Fujimoto, T.; Kuga, Y. Scalable and template-free production of mesoporous calcium carbonate and its potential to formaldehyde adsorbent. *J. Nanopart. Res.* **2014**, *16*, 2266.
- (48) Bots, P.; Benning, L. G.; Rodriguez-Blanco, J.-D.; Roncal-Herrero, T.; Shaw, S. Mechanistic Insights into the Crystallization of Amorphous Calcium Carbonate (ACC). *Cryst. Growth Des.* **2012**, *12*, 3806–3814.
- (49) Vacassy, R.; Lemaitre, J.; Hofmann, H.; Gerlings, J. H. Calcium carbonate precipitation using new segmented flow tubular reactor. *AIChE J.* **2000**, *46*, 1241–1252.
- (50) Behrens, G.; Kuhn, L. T.; Ubic, R.; Heuer, A. H. RAMAN-SPECTRA OF VATERITIC CALCIUM-CARBONATE. *Spectrosc. Lett.* **1995**, *28*, 983–995.
- (51) Balz, M.; Therese, H. A.; Li, J. X.; Gutmann, J. S.; Kappl, M.; Nasdala, L.; Hofmeister, W.; Butt, H. J.; Tremel, W. Crystallization of vaterite nanowires by the cooperative interaction of tailor-made nucleation surfaces and polyelectrolytes. *Adv. Funct. Mater.* **2005**, *15*, 683–688.
- (52) Kontoyannis, C. G.; Vagenas, N. V. Calcium carbonate phase analysis using XRD and FT-Raman spectroscopy. *Analyst* **2000**, *125*, 251–255.
- (53) Armstrong, J. K.; Wenby, R. B.; Meiselman, H. J.; Fisher, T. C. The hydrodynamic radii of macromolecules and their effect on red blood cell aggregation. *Biophys. J.* **2004**, *87*, 4259–4270.
- (54) Ogino, T.; Suzuki, T.; Sawada, K. The formation and transformation mechanism of calcium carbonate in water. *Geochim. Cosmochim. Acta* **1987**, *51*, 2757–2767.
- (55) Bouby, M.; Geckeis, H.; Geyer, F. W. Application of asymmetric flow field-flow fractionation (AsFFFF) coupled to inductively coupled plasma mass spectrometry (ICPMS) to the quantitative characterization of natural colloids and synthetic nanoparticles. *Anal. Bioanal. Chem.* **2008**, *392*, 1447–1457.
- (56) Fanun, M. *Colloids in biotechnology*; CRC Press: Boca Raton, FL, 2011.
- (57) Uhlig, K.; Madaboosi, N.; Schmidt, S.; Jäger, M. S.; Rose, J.; Duschl, C.; Volodkin, D. V. 3d localization and diffusion of proteins in polyelectrolyte multilayers. *Soft Matter* **2012**, *8*, 11786–11789.
- (58) Paulraj, T.; Feoktistova, N.; Velk, N.; Uhlig, K.; Duschl, C.; Volodkin, D. Microporous Polymeric 3D Scaffolds Templated by the Layer-by-Layer Self-Assembly. *Macromol. Rapid Commun.* **2014**, *35*, 1408–13.
- (59) Sergeeva, A.; Feoktistova, N.; Prokopovic, V.; Gorin, D.; Volodkin, D. Design of Porous Alginate Hydrogels by Sacrificial CaCO<sub>3</sub> Templates: Pore Formation Mechanism. *Adv. Mater. Interfaces* **2015**, DOI: 10.1002/admi.201500386.
- (60) Sergeeva, A. S.; Gorin, D. A.; Volodkin, D. V. In-Situ Assembly of Ca-Alginate Gels with Controlled Pore Loading/Release Capability. *Langmuir* **2015**, *31*, 10813–10821.
- (61) Volodkin, D.; von Klitzing, R. Competing mechanisms in polyelectrolyte multilayer formation and swelling: Polycation–polyanion pairing vs. polyelectrolyte–ion pairing. *Curr. Opin. Colloid Interface Sci.* **2014**, *19*, 25–31.
- (62) Volodkin, D.; Skirtach, A.; Mohwald, H. LbL Films as Reservoirs for Bioactive Molecules. In *Bioactive Surfaces*; Börner, H. G., Lutz, J. F., Eds.; Springer-Verlag: Berlin, 2011; Vol. 240, pp 135–161.
- (63) Vikulina, A. S.; Anissimov, Y. G.; Singh, P.; Prokopovic, V. Z.; Uhlig, K.; Jaeger, M. S.; von Klitzing, R.; Duschl, C.; Volodkin, D. Temperature effect on the build-up of exponentially growing polyelectrolyte multilayers. An exponential-to-linear transition point. *Phys. Chem. Chem. Phys.* **2016**, *18*, 7866–74.